

# Poglavje 1

## Povzetek doktorskega dela

### 1.1 Uvod

Fizika delcev je eden od stebrov fizike, z močnimi koreninami, ki segajo vse do začetka 20. stoletja. Natančni eksperimenti in preverljiva teorija so pokazali, da vesolje sestoji iz osnovnih delcev in nosilcev interakcij. Osnovne delce delimo na kvarke ( $u, d, s, c, b, t$ ) in leptone, ki so nadaljnje razdeljeni na nabite leptone ( $e, \mu, \tau$ ) in pa nevtrine ( $\nu_e, \nu_\mu, \nu_\tau$ ). Nosilci treh (od štirih) osnovnih interakcij, s katerimi se ukvarjamo na tem področju, so fotoni ( $\gamma$ ) za elektromagnetno, gluoni ( $g$ ) za močno in nabiti- ( $W^\pm$ ) ter nevtralni ( $Z^0$ ) bozoni za šibko interakcijo. Vsi delci in njihovi zrcalni partnerji, antidelci (označeni z  $^-$ ), imajo maso, ki jim jo določa Higgsov bozon ( $H$ ). Vse delce ter interakcije med njimi opisuje Standardni model, ki je osrednja teorije fizike visokih energij. Kvarke lahko združujemo v kombinacije oblike  $q_1 q_2 q_3$  (hadroni) ali pa  $q_1 \bar{q}_2$  (mezoni), med katere sodijo tudi protoni in nevtroni, ki jih opazimo v naravi. Poleg omenjenih dolgo-živečih delcev pa obstajajo tudi težji, manj stabilni delci, ki preko zgoraj naštetih interakcij razpadejo v lažje, stabilnejše. Raziskovanje takšnih procesov s pomočjo pospeševalnikov in trkalnikov nam omogoča spoznavanje zakonov vesolja danes pa vse do njegovega začetka.

Osrednji del doktorske disertacije predstavlja meritve razpadov mezonov  $B$ , delcev, ki so sestavljeni iz težkega kvarka  $b$  in enega od lahkkih kvarkov  $u$  ali  $d$ . Ena bolj presegajočih lastnosti vesolja je kršitev simetrije  $CP$ , t.j. kombinacije simetrij konjugacije naboja ( $C$ ) in prostorske inverzije ( $P$ ). Simetrija  $CP$  nakazuje, da so fizikalni procesi delcev in zrcalni procesi antidelcev enaki, kar pa danes vemo, da ne drži v celoti in poznamo procese, ki to simetrijo kršijo. Kršitev simetrije  $CP$  je tesno povezana s šibko interakcijo, to pa predstavlja našo motivacijo za študijo mezonov  $B$ , saj šibki razpadi predstavljajo večji del vseh razpadov mezonov  $B$ .

Edinstvena lastnost šibke interakcije je, da lahko spreminja tip oziroma t.i. okus kvarkov, medtem ko ga ostale interakcije ohranjajo. Takšni procesi so opisani s prehodno matriko

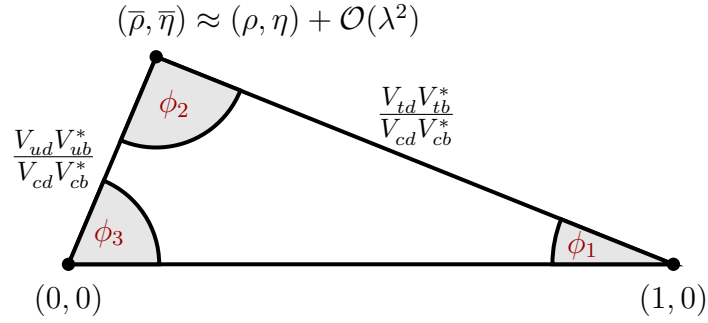
28 CKM (Cabibbo-Kobayashi-Maskawa) [1, 2]

$$V_{CKM} = \begin{bmatrix} V_{ud} & V_{us} & V_{ub} \\ V_{cd} & V_{cs} & V_{cb} \\ V_{td} & V_{ts} & V_{tb} \end{bmatrix}. \quad (1.1)$$

29 Unitarnost matrike CKM nam omogoča, da iz nje izluščimo matematične identitete, od  
30 katerih je ena pomembnejših

$$V_{ud}V_{ub}^* + V_{cd}V_{cb}^* + V_{td}V_{tb}^* = 0, \quad (1.2)$$

31 poznana pod imenom unitarni trikotnik, saj predstavlja zaključen vektor treh točk v  
32 kompleksni ravnini, kot prikazuje Slika 1.1. Parametri matrike CKM niso določljivi  
33 s strani teorije, temveč jih moramo določiti z eksperimentalnimi meritvami tako, da  
34 najdemo procese, ki so tesno povezani s stranicami in koti unitarnega trikotnika. Na  
35 tak način lahko preverimo, če je oblika trikotnika konsistentna, kar predstavlja dober  
36 test Standardnega modela, oziroma če so potencialno prisotni kakšni novi procesi, ki  
37 jih še ne poznamo, in jih kolektivno imenujemo "nova fizika". Dodatna motivacija za  
38 študijo mezonov  $B$  je ta, da velik delež njihovih razpadov predstavlja koristne procese  
39 za meritev unitarnega trikotnika.



Slika 1.1: Unitarni trikotnik s parametri  $\lambda$ ,  $\eta$ ,  $\rho$  and  $A$  (slednji ni prikazan), ki predstavljajo proste parametre matrike CKM.

40 Procesi, ki jih študiramo v tej analizi, so tesno povezani z elementom  $V_{ub}$  matrike CKM,  
41 saj le-ta opisuje prehode kvarkov  $b \rightarrow c$ . Od vseh elementov, je absolutna vrednost  
42 tega elementa najmanjša, relativna napaka pa največja, zato meritve iz tega področja  
43 potencialno omogočajo največ izboljšave. Takšni prehodi kvarkov so prisotni v nearobnih  
44 (t.j. brez kvarkov  $c$ ) semi-leptonskih razpadih mezonov  $B$  oblike

$$B^+ \rightarrow X_u^0 \ell^+ \nu_\ell, \quad (1.3)$$

45 kjer  $X_u^0$  predstavlja nečarnobne mezone,  $\ell$  pa je eden od nabitih leptonov. Frekvenco  
46 razpadov, ki je tesno povezana z elementom  $V_{ub}$ , opišemo z enačbo

$$d\Gamma \propto G_F^2 |V_{ub}|^2 |L^\mu \langle X_u | \bar{u} \gamma_\mu \frac{1}{2} (1 - \gamma_5) b | B \rangle|^2, \quad (1.4)$$

47 kjer  $G_F$  predstavlja Fermijevo konstanto,  $L^\mu$  leptonski tok, izraz v Diracovih oklepajih  
 48 pa hadronski tok. V takšnih prehodih  $|V_{ub}|^2$  predstavlja verjetnost za prehod  $b \rightarrow u$ .

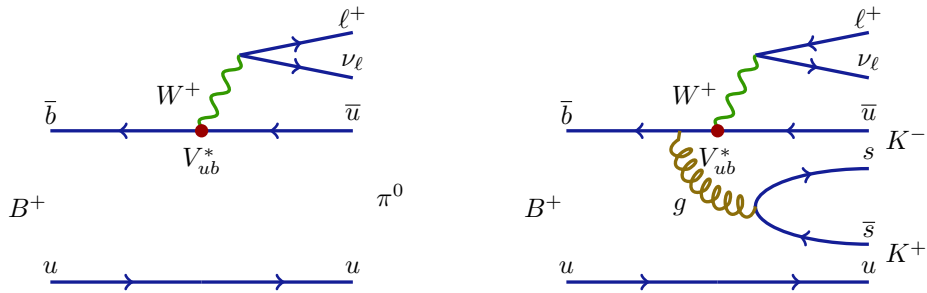
Meritev elementa  $V_{ub}$  je možna na ekskluziven in inkluziven način, kjer pri prvi metodi opravljamo meritve v specifično definirana končna stanja, kot na primer  $B \rightarrow \pi \ell \nu$ , pri drugi metodi pa opravljamo meritev s kupno končno stanje oblike  $B \rightarrow X_u \ell \nu$ . Obe metodi potekata preko različnih pristopov in se soočata z različnimi težavami, kar pomeni, da sta oba končna rezultata nekorelirana. Rezultata obeh meritev imata tudi zelo podobno natančnost, medtem ko se srednja vrednost le deloma ujema. Rezultata se razlikujeta s signifikanco  $3\sigma$ , kar predstavlja večjo težavo znotraj področja. Trenutni svetovni povprečji [3] ekskluzivne (iz razpadov  $B^0 \rightarrow \pi^- \ell^+ \nu$ ) in inkluzivne meritve (GGOU kolaboracija [4]) sta

$$|V_{ub}|_{\text{e.}} = (3.65 \pm 0.09 \pm 0.11) \times 10^{-3}, \quad (1.5)$$

$$|V_{ub}|_{\text{i.}}^{\text{GGOU}} = (4.52 \pm 0.15 \pm_{-0.14}^{+0.11}) \times 10^{-3}, \quad (1.6)$$

49 kjer prva in druga napaka predstavljata eksperimentalno in teoretsko napako. Rezultati  
 50 inkluzivnih meritev so praviloma večji kot rezultati ekskluzivnih. Razlogov za neujema-  
 51 nje je lahko več, od nepoznanih napak pri eksperimentu ali teoriji, do prispevkov nove  
 52 fizike.

53 V tej analizi se osredotočamo na enega od možnih razlogov za zgoraj omenjeno neujema-  
 54 nje, konkretnije za razpad  $B^+ \rightarrow K^+ K^- \ell^+ \nu$ , ki je strukturno precej podoben razpadu  
 55  $B \rightarrow \pi \ell \nu$  za razliko produkcije para kvarkov  $s\bar{s}$  ki se potem hadronizira v nove delce, kot  
 56 prikazuje Slika 1.2. V inkluzivnih meritvah nečarobnih semi-leptonskih razpadov me-  
 57 zonov  $B$  se standardno uporablja  $K$ -veto, t.j. selekcija, kjer zahtevamo, da v končnem  
 58 stanju nimamo mezonov  $K$  (sestava  $q\bar{s}$ ,  $q \in [u, d]$ ), poznanih tudi pod imenom kaoni.  
 59 Kaoni v končnem stanju nakazujejo na pogost prehod kvarkov  $b \rightarrow c \rightarrow s$ , ki pa jih  
 60 hočemo v analizah prehodov  $b \rightarrow u$  zatreti. V primeru naše analize imamo v končnem  
 61 stanju 2 kaona s preходом  $b \rightarrow u$ , kar pomeni, da takšni razpadi niso upoštevani v  
 62 inkluzivnih meritvah, čeprav bi morali biti. Cilj študije je določiti pogostost razpadov  
 63  $B^+ \rightarrow K^+ K^- \ell^+ \nu$  s preходом  $b \rightarrow u$  in s tem oceniti, kakšen potencialen efekt ima  
 64 lahko neupoštevanje teh razpadov na inkluzivno meritev elementa  $V_{ub}$ . V nadaljevanju  
 65 bo razpad  $B^+ \rightarrow K^+ K^- \ell^+ \nu$  zaradi enostavnosti zapisan kot  $B \rightarrow K K \ell \nu$ .



Slika 1.2: Feynmanovi diagrami za razpada  $B^+ \rightarrow \pi^0 \ell^+ \nu_\ell$  (levo) in  $B^+ \rightarrow K^- K^+ \ell^+ \nu_\ell$  (desno).

## 1.2 Experimentalna postavitve

Podatki, uporabljeni v tej analizi, so bili ustvarjeni pri trkih elektronov  $e^-$  in pozitronov  $e^+$  v pospeevalniku KEKB in zajeti z detektorjem Belle. Eksperiment je trajal od leta 1999 do 2010 pod okriljem znanstvene organizacije KEK v mestu Tsukuba na Japonskem. Trki delcev so se dogajali pri energiji, ki je ustrezala masi resonance  $\Upsilon(4S)$ , (sestava  $b\bar{b}$ ). V tem delu disertacije sta opisana pospeevalnik in detektor, podrobnejši opis pa se nahaja v literaturah [5] in [6].

### 1.2.1 Trkalnik KEKB

KEKB je asimetričen trkalnik delcev  $e^+e^-$ , ki potujejo po obroih s premerom 3 km v gruah. V središču detektorja grui elektronov z energijo 8 GeV in pozitronov z energijo 3.5 GeV trita pod kotom 22 mrad. Skupna invariantna masa trka ustreza masi resonance  $\Upsilon(4S)$

$$E_{CM} = 2\sqrt{E_{e^+}E_{e^-}} = m_{\Upsilon(4S)}c^2 \approx 10.58 \text{ GeV}. \quad (1.7)$$

Dele mezonov  $\Upsilon(4S)$  razpade preko zelo istega kanala v dva praktino mirujoča mezona  $B$ , kar tej in v podobnih analizah pogosto izkoriamo, saj je začetno stanje dobro poznano.

Trkalnik je v asu obratovanja zajel količino podatkov, ki ustreza integrirani luminoznosti  $1041 \text{ fb}^{-1}$ , od katere okoli  $711 \text{ fb}^{-1}$  predstavlja podatke, zajete pri energiji 10.58 GeV, t.j. masi resonance  $\Upsilon(4S)$ . Slednja vrednost integrirane luminoznosti ustreza tevilu  $771 \times 10^6$  parov  $B\bar{B}$  mezonov.

### 1.2.2 Detektor Belle

Detektor Belle je magnetni masni spektrometer, ki pokriva večji del prostorskega kota. Njegov namen je, da detektira delce, ki se gibljejo v magnetnem polju 1.5 T in so potomci trkov  $e^+e^-$ . Cilj je določiti energijo in gibalno količino delcev, kar dosežemo preko detektorskih podsistemov, ki so okoli interakcijske točke postavljeni v plasteh. Detektor pokriva polarni kot med  $17^\circ \leq \theta \leq 150^\circ$ , med tem ko je azimutni kot pokrit v celoti, kar skupaj predstavlja 92% pokritost polnega prostorskega kota.

#### Silikonski detektor verteksov

Silikonski detektor verteksov je postavljen najbližje interakcijski točki. Sestavljen je iz dvostranskih silikonskih detektorjev, ki podajajo 2D informacijo o prehodih nabitih delcev z natančnostjo okoli  $100 \text{ } \mu\text{m}$ . To nam omogoča določitev točk razpada (verteksov) kratko-živečih delcev.

## Osrednja potovalna komora

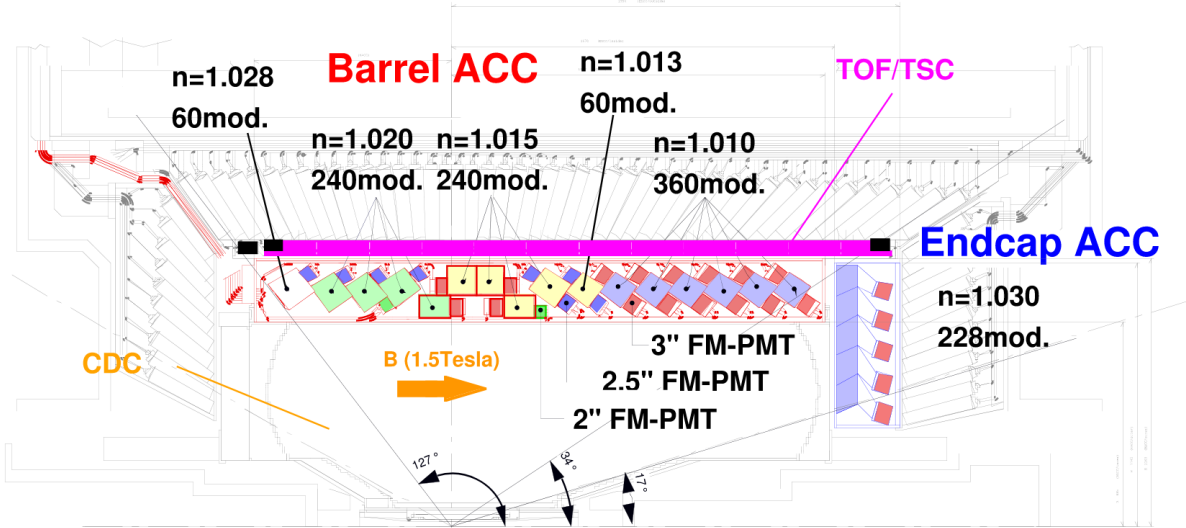
Osrednja potovalna komora je sestavljena iz mnogo žic, napeljanih skozi mešanico plina. Komora tako meri sledi nabitih delcev, ki potujejo skozi magnetno polje v detektorju. Preko sledi lahko določimo informacijo o gibalni količini delca, hkrati pa v območju gibalne količine pod  $0.8 \text{ GeV}/c$  služi tudi za njihovo identifikacijo.

## Merilec časa preleta

Merilec časa preleta meri časovno razliko od trka pa do preleta delca skozi enega od scintilatorjev tega podsistema. Namen je identifikacija delcev v območju gibalnih količin  $0.8 \text{ GeV}/c < p < 1.2 \text{ GeV}/c$ , še posebej kaonov  $K^\pm$  in pionov  $\pi^\pm$ . Pri isti gibalni količini zaradi različnih mas delcev dobimo različne case preleta, kar lahko uporabimo za določitev njihove mase. Časovna resolucija tega podsistema je boljša kot ali enaka  $100 \text{ ps}$ .

## Pragovni števec sevanja Čerenkova

TOF is not capable of performing good PID above  $1.2 \text{ GeV}/c$  momentum, since  $\beta$  is almost equal to 1. For higher momenta in the region  $1.0 \text{ GeV}/c < 4.0 \text{ GeV}/c$ , the ACC is introduced. It is a threshold-type Cherenkov counter which utilizes the fact that particles emit Cherenkov light if the particle speed is greater than the speed of light in the passing medium. ACC is introduced in the barrel region with 960 separate modules, covering a polar angle of  $34^\circ < \theta < 127^\circ$  and 228 modules in the forward end-cap region, with the polar angle coverage of  $17^\circ < \theta < 34^\circ$ . Each ACC module consists of an aluminum encased block of silica aerogel and one or two fine-mesh PMTs encased on each block to detect Cherenkov light pulses. Due to the polar angle dependence of the particle momentum, 6 different refractive indices are chosen for the aerogel material, ranging from 1.010 up to 1.030 and are controlled within 3% precision. The layout of the ACC is shown in Figure 1.3.

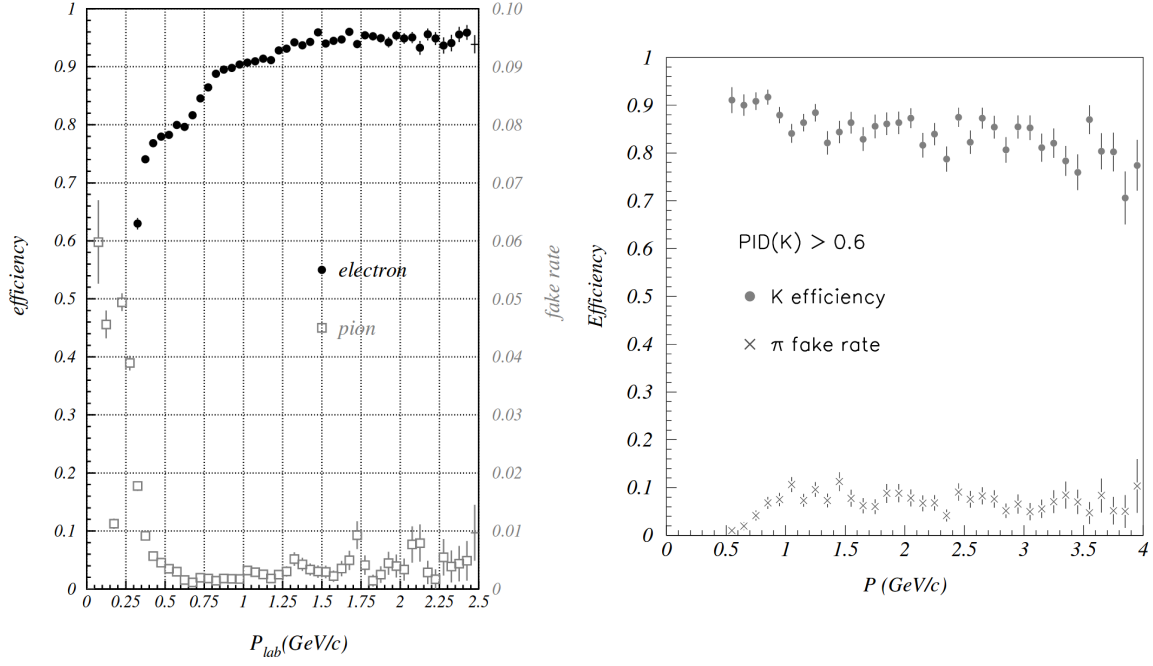


Slika 1.3: Cross-sectional view of the CDC (inner most), ACC and TOF (outer most) detectors [6].

121 The threshold velocity  $\beta$  of a given particle for Cherenkov radiation is

$$\beta \leq \frac{1}{n}, \quad (1.8)$$

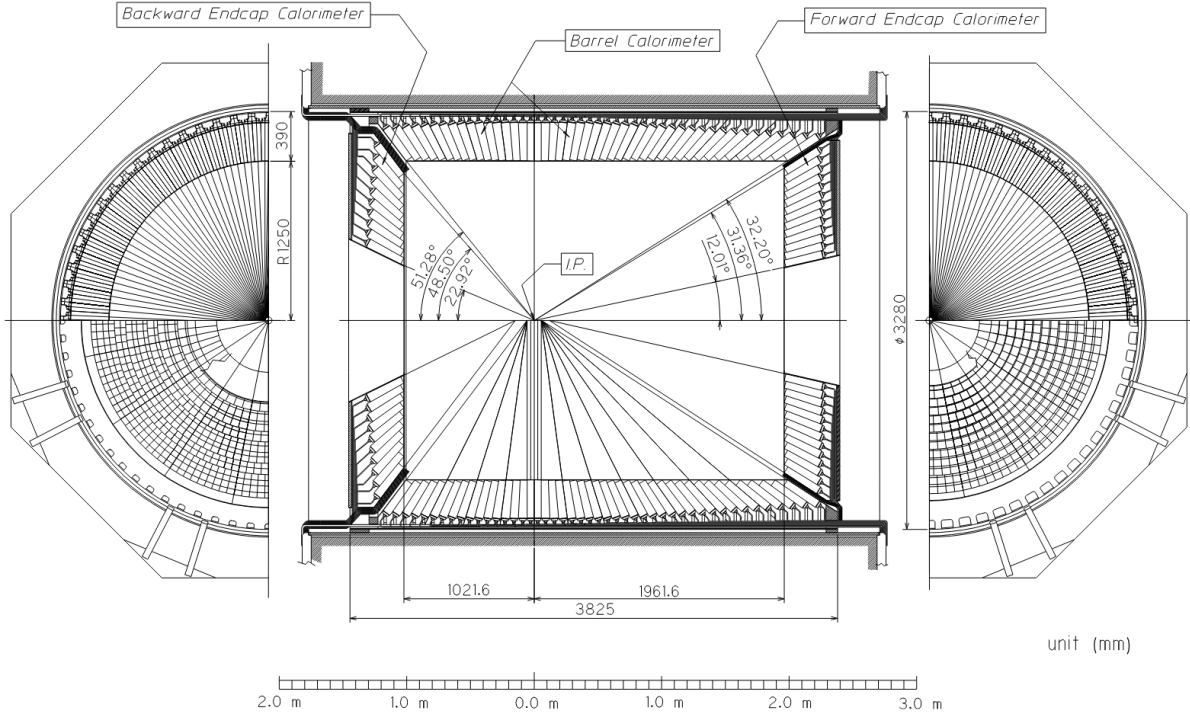
122 where  $n$  is the refractive index of the medium. The refractive indices in the ACC are  
 123 such that, due to different masses, pions will emit Cherenkov light and kaons will not,  
 124 due to different masses of the particles. Using the PID of ACC, along with other sub-  
 125 system PID info, the electron identification efficiency in the momentum range above  
 126 1 GeV/ $c$  is equal to or above 90% while the pion fake rate, the probability of wrongly  
 127 identifying pions as electrons, to be around 0.2 - 0.3%. Similarly for kaons, kaon ID  
 128 efficiency is equal to 80% for most of the momentum region up to 4 GeV/ $c$ , while pion  
 129 fake rate remains below 10%. Figure 1.4 shows the electron and kaon efficiencies and  
 130 the corresponding pion fake rates as a function of particle momenta.



Slika 1.4: Electron identification efficiency and fake rate for charged pions (left) and similarly for kaons (right). Note the different scales for the electron efficiency and fake rate in the former case [6].

## Electromagnetic Calorimeter

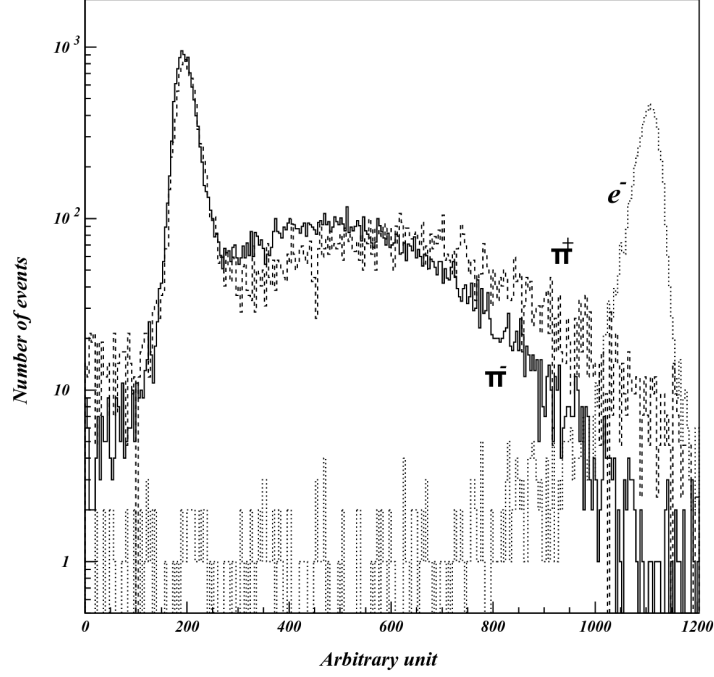
Measurement of position and energy deposit of particles is performed in the ECL, especially for electrons and photons, where the latter are not measured by any of the subsystems described so far. It also provides complimentary particle identifications for electrons versus pions. The calorimeter consists of a highly segmented array of thallium-doped caesium iodide (CsI(Tl)) in the form of tower-shaped crystals, each pointing towards the IP. Each crystal is about 30 cm long with a width from 44.5 mm to 65 mm in the barrel, and from 44.5 mm to 82 mm in the end-caps. Out of a total of 8736 crystals with a total mass of about 43 tons, 6624 of them are positioned in the barrel region and 1152 (960) in the forward (backward) end-caps. The inner radius of the barrel section is about 1.25 m, while the end-caps are positioned at  $-1.0$  m and  $2.0$  m from the IP in direction of the  $z$  axis. The polar angle coverage of the barrel region is  $32.2^\circ < \theta < 128.7^\circ$ , and for the end-caps  $12.4^\circ < \theta < 31.4^\circ$  and  $130.7^\circ < \theta < 155.1^\circ$ . Figure 1.5 shows the layout of the barrel and end-caps ECL.



Slika 1.5: Overall configuration of the ECL [6].

145 When an electron or a photon hits a crystal, it produces an electromagnetic shower,  
 146 a result of the bremsstrahlung and pair-production effects. Heavier charged particles  
 147 do not interact in the same way and deposit only a small amount of energy by ioniza-  
 148 tion effects. The information from the ECL, compared with momentum measurements  
 149 provided by the CDC, enables the identification of electrons. The distribution of the  
 150 deposited energy for different particles is shown in Figure 1.6. The probability of misi-  
 151 dentifying an electron as a pion is approximately 5% for momenta less than 1 GeV/ $c$ ,  
 152 and less than 1% for momenta above 2 GeV/ $c$ .





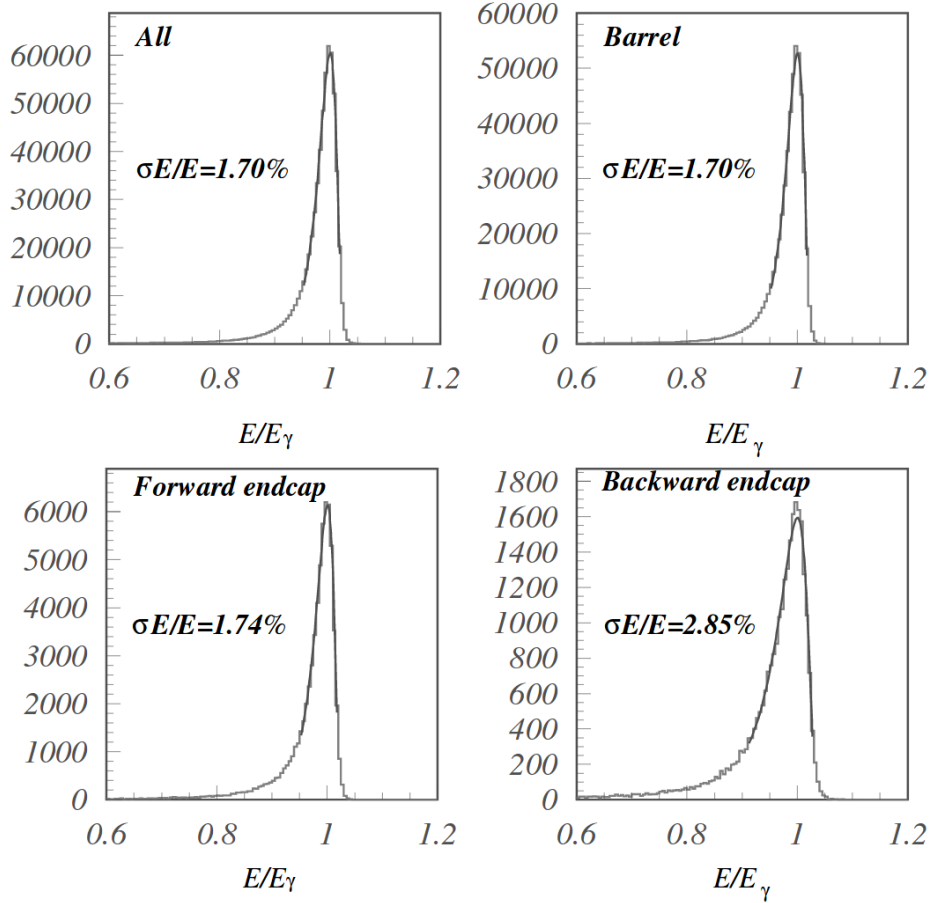
Slika 1.6: Distribution of the energy deposit by electrons and charged pions at 1 GeV/ $c$  momentum [6].

For ECL calibration,  $e^+e^- \rightarrow e^+e^-$  and  $e^+e^- \rightarrow \gamma\gamma$  events were used. The average energy resolution was achieved to be 1.7% for the barrel ECL, and 1.74% and 2.85% for the forward and backward ECL, respectively, as shown in Figure 1.7. These value are in good agreement with Monte Carlo predictions. Worse energy resolution in backward end-cap is due to the lower photon energy, which results in larger effects of passive material in front of the calorimeter [7]. The energy resolution as a function of energy can be obtained via the following relation

$$\frac{\sigma_E}{E} = \frac{0.0066\%}{(E/1 \text{ GeV})} \oplus \frac{1.53\%}{(E/1 \text{ GeV})^{1/4}} \oplus 1.18\%, \quad (1.9)$$

while the resolution of the position measurement is

$$\sigma_{pos} = 0.27 \text{ mm} + \frac{3.4 \text{ mm}}{(E/1 \text{ GeV})^{1/2}} + \frac{1.8 \text{ mm}}{(E/1 \text{ GeV})^{1/4}}. \quad (1.10)$$

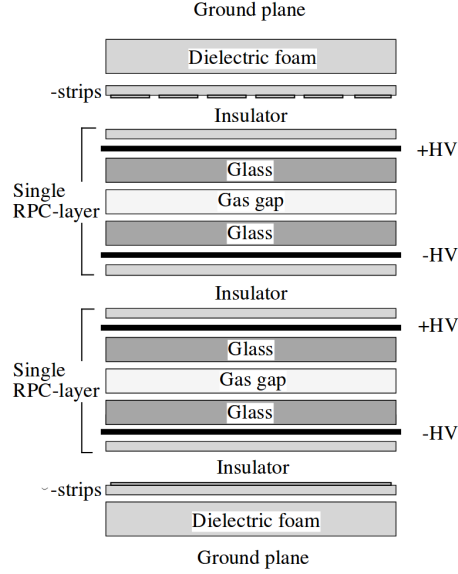


Slika 1.7: Reconstructed energy distribution for  $e^+e^- \rightarrow \gamma\gamma$  events for overall, barrel, forward and backward end-cap calorimeters [6].

## $K_L^0/\mu$ Detector

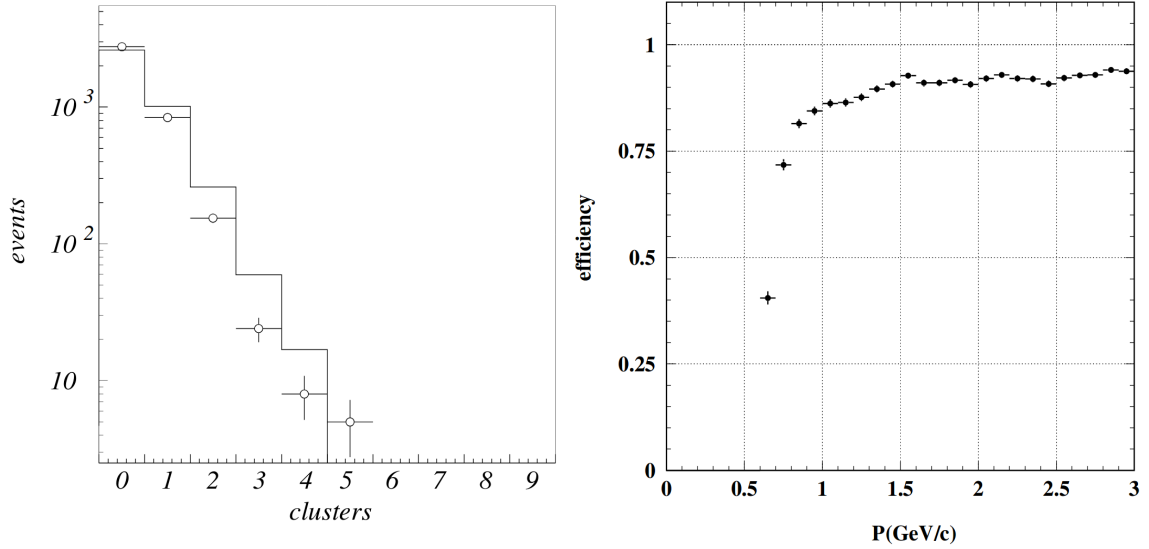
The KLM detector is used for detection of high-penetration particles such as  $K_L^0$  and  $\mu$  for momenta larger than 0.6 GeV/c. The setup covers the polar angle of  $20^\circ < \theta < 155^\circ$ . Detection of  $K_L^0$  particles is troublesome, since they are neutral and have a small material interaction probability, therefore a lot of material is needed in the KLM. To provide detection of both kinds of particles, hadronic and neutral, as well as electromagnetically and hadronically interacting, the KLM is constructed as a sampling calorimeter, which consists of 15 layers of 3.7 cm thick resistive-plate counters (RPC) with 14 layers of 4.7 cm thick iron plates between them. A single RPC module consists of two parallel plate electrodes, two glass panels, and gas in between. A charged particle passing the gas gap initiates a local discharge of the plates, which in turn induces signal to record the time and location of ionization. This is possible since the resistivity of the glass surface is high, so the discharge occurs locally. Hadrons interacting with the iron plates may produce a shower of ionizing particles, which are then also detected by the RPCs.

175 The KLM is located outside of superconducting solenoid and the iron plates of the KLM  
 176 serve a dual role as the flux return for the magnetic field. Figure 1.8 shows a cross-section  
 177 of an RPC superlayer, consisting of an RPC pair.



Slika 1.8: Cross-section of an RPC superlayer, consisting of an RPC pair [6].

178 The  $K_L^0$  particle can be distinguished from other charged hadrons because they have  
 179 no matched track in the CDC. The flight direction can also be inferred from the hit  
 180 locations in the consecutive RPCs. Tracks of charged particles measured in CDC are  
 181 extrapolated into KLM and clusters within  $15^\circ$  of an extrapolated charged particle track  
 182 are excluded from  $K_L^0$  cluster candidates. On the other hand, muons with matched CDC  
 183 tracks are able to reach the KLM if their momentum is larger than  $0.5 \text{ GeV}/c$ . They  
 184 do not interact strongly and do not produce hadronic showers in the KLM, which serves  
 185 as a handle on the muon identification. Figure 1.9 (left) shows the number of neutral  
 186 clusters per event and a Monte Carlo simulation of the predicted number of  $K_L^0$  clusters  
 187 per event. The average number of  $K_L^0$  clusters per event is 0.5. The agreement with  
 188 the prediction gives us the confidence that the detector and our reconstruction software  
 189 are performing correctly. Figure 1.9 (right) shows the muon detection efficiency as a  
 190 function of momentum and shown for a likelihood cut of 0.66, where muon likelihood is  
 191 based on the comparison of the measured range of a particle with the predicted range  
 192 for a muon. Based on  $K_S \rightarrow \pi^+\pi^-$  events, a muon identification efficiency of better than  
 193 90% is determined, with a pion fake rate of less than 5% for particles with momenta  
 194 more than  $1.5 \text{ GeV}/c$  and a likelihood cut of 0.66.



Slika 1.9: Number of neutral clusters per event in KLM (left) and muon detection efficiency as a function of momentum in KLM (right) [6].

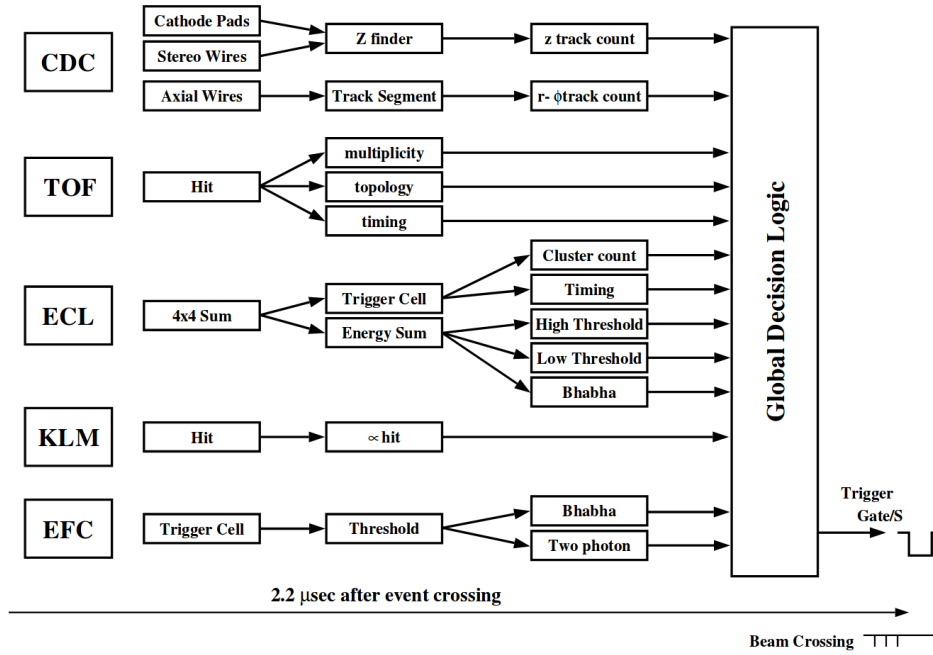
Cosmic ray events have been used to determine efficiency and resolution of the KLM, with an overall efficiency typically over 98%. The temporal and spatial resolution of the KLM are few ns and about 1.2 cm, respectively. The latter corresponds to an angular resolution from the interaction point of better than 10 mrad.

In order to to detector calibration and proper luminosity measurements, we need to accumulate samples of Bhabha and  $\gamma\gamma$  scattering. Otherwise, as shown in Table ??, the cross-section for physics events of interest is reasonably small. During normal operation (luminosity of  $L = 10 \times 10^{34} \text{ cm}^{-2}\text{s}^{-1}$ ) the total event rate is around 200 Hz, which is well below the data acquisition (DAQ) limit of 500 Hz. Out of this rate, 100 Hz are physically interesting events, which include also two photon events, Bhabha scattering and  $\mu$  pair production, besides hadronic events from  $B\bar{B}$  pair events. In order to discard events which are not interesting for physics analyses, we use a trigger system by appropriately applying restrictive conditions. This section describes the necessary procedures and equipment to successfully do so.

## Trigger System

The trigger system operates by immediately eliminating events that are not of interest, so that the amount of stored data is within the 500 Hz frequency limit, while the efficiency for physics events of interest is kept high. Events which pass the triggers are then stored, otherwise discarded. The Belle trigger system consists of three stages, Level-1 (L1) online hardware trigger, Level-3 (L3) online software trigger and Level-4 (L4) offline software trigger.

L1 trigger is the first stage of the trigger system, which consists of multiple sub-detector triggers, all connected to a central trigger system called the Global Decision Logic (GDL), as schematically shown in Figure 1.10. Each sub-detector trigger works on a principle of either a track trigger or an energy trigger. In the former case the triggers discard events not meeting conditions based on the number of reconstructed tracks or track hits, while the latter is based on the total energy deposit and counting of crystal hits. Each sub-detector processes the event information and provides it to the GDL, where all the information is combined and the current event is characterized. The information from the sub-detector triggers reaches the GDL within  $1.85 \mu\text{s}$  after the collision, and the final trigger signal is provided within at a fixed  $2.2 \mu\text{s}$  latency. The combined efficiency from the L1 trigger is greater than 99.5% for hadronic events.



Slika 1.10: The Level-1 trigger system for the Belle detector [6].

After passing L1 trigger, the L3 discards background events from the software-wise perspective. L3 is an online software trigger which performs a simple, but fast reconstruction of the event. Events with at least one track satisfying the impact parameter condition  $|dz| < 5.0 \text{ cm}$  and with a total energy deposit in the ECL more than  $1 \text{ GeV}/c$  are selected. The L3 trigger reduces the event rate by 50%, with a 99% efficiency for hadronic events.

After passing the L3 trigger, the events are recorded on tapes. However, these data still contain many events from the beam background. To reduce the background events even further, they are required to pass the L4 offline software filtering. At the same time, high efficiencies for signal events is still required. Events must satisfy the following conditions

- 237     • have at least one track with  $p_T > 300$  MeV/ $c$  and impact parameters  $|dr| < 1.0$  cm  
238         and  $|dz| < 4.0$  cm,
- 239     • have total energy deposit in the ECL must greater than 4 GeV.

240   Approximately 27% of triggered events are passed through L4, while keeping an almost  
241   full efficiency for hadronic events. Events that pass the L4 trigger are fully reconstructed  
242   and stored to the DST. Overall, the efficiency of hadronic events after all trigger stages  
243   is measured to be more than 99%, which is more than the requirements from physics  
244   analyses.

## 245   **1.3 Postopek analize**

## 246   **1.4 Sistematske negotovosti**

## 247   **1.5 Končni rezultat**